Nested dust shells around the Wolf–Rayet binary WR 140 observed with JWST

Ryan M. Lau [1] ✉, Matthew J. Hankins[2], Yinuo Han[3], Ioannis Argyriou [4], Michael F. Corcoran[5,6], Jan J. Eldridge [7], Izumi Endo [8], Ori D. Fox [9], Macarena Garcia Marin[10,11], Theodore R. Gull [9,12], Olivia C. Jones [13], Kenji Hamaguchi[5,14], Astrid Lamberts[15,16], David R. Law[9], Thomas Madura[17], Sergey V. Marchenko[18,19], Hideo Matsuhara[20], Anthony F. J. Moffat [21,22], Mark R. Morris [23], Patrick W. Morris [24], Takashi Onaka [8,25], Michael E. Ressler [26], Noel D. Richardson [27], Christopher M. P. Russell [28], Joel Sanchez-Bermudez [29,30], Nathan Smith [31], Anthony Soulain [32], Ian R. Stevens [33], Peter Tuthill[34], Gerd Weigelt [35], Peredur M. Williams [36] and Ryodai Yamaguchi[20,37]

Massive colliding-wind binaries that host a Wolf–Rayet (WR) star present a potentially important source of dust and chemical enrichment in the interstellar medium. However, the chemical composition and survival of dust formed from such systems is not well understood. The carbon-rich Wolf–Rayet binary WR 140 presents an ideal astrophysical laboratory for investigating these questions, given its well-defined orbital period and predictable dust-formation episodes every 7.93 years around periastron passage. We present observations from our Early Release Science programme (ERS 1349) with the James Webb Space Telescope Mid-Infrared Instrument (MIRI) Medium-Resolution Spectrometer and Imager that reveal the spectral and spatial signatures of nested circumstellar dust shells around WR 140. MIRI medium-resolution spectroscopy of the second dust shell and Imager detections of over 17 shells formed throughout approximately the past 130 years confirm the survival of carbonaceous dust grains from WR 140 that are probably carriers of 'unidentified infrared'-band features at 6.4 and 7.7 μm. The observations indicate that dust-forming carbon-rich Wolf–Rayet binaries can enrich the interstellar medium with organic compounds and carbonaceous dust.

Some of the first carbonaceous dust grains and organic material in the Universe may have been produced in the compressed, chemically enriched winds of massive, evolved colliding-wind binaries hosting a Wolf–Rayet (WR) star of the carbon-rich (WC) subtype[1–3]. In the hostile environment around these massive and evolved stars[4], dust is produced from the compressed gas in the wind collision region where the stronger stellar wind from the WR star interacts with the stellar wind of an OB star companion[5–7]. Galactic colliding-wind WC binaries with resolvable circumstellar dust nebulae therefore provide important laboratories for studying this dust-formation process, where observations over the past few decades have demonstrated how dust formation is regulated by the orbit of the binary system[2,5,6,8]. However, the chemical signatures of dust grains formed in colliding-wind WC binaries[9], and the survival of these grains as they propagate into the interstellar medium (ISM) in their harsh radiative stellar environment, are not well understood.
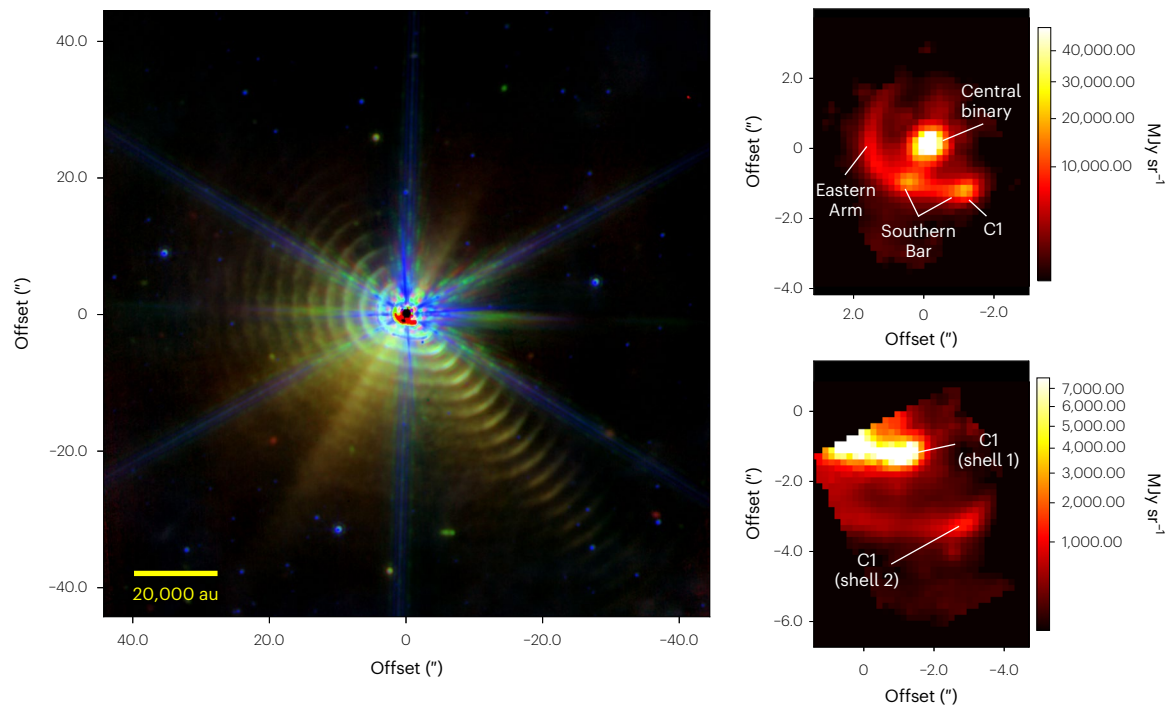
Fig. 1 | JWST/MIRI observations of WR 140. Left: false-colour JWST/MIRI Imager observations of WR 140 taken with the F770W, F1500W and F2100W filters that correspond to blue, green and red, respectively. Eight symmetric diffraction spikes are seen around the saturated core of WR 140 (at the origin) that exhibit bluer colours than the dust emission. Right: JWST/MIRI MRS spectral data cube images of WR 140 from Channel 2 at 8.01 μm taken at two different positions that cover the central binary and shell 1 (Offset 1, top) and shells 1 and 2 (Offset 2, bottom) shown in a square-root stretch. The central binary and bright dust emission features are labelled in the MRS data cube images.

Arguably the best example of 'episodic' dust formation in colliding winds is the WR binary WR 140 (also known as HD 193793), a carbon-rich evolved massive star of subtype WC7 in a highly eccentric ($e = 0.89$), 2,895 d (7.93 yr) mutual orbit around an early-type O5.5fc star[10–12]. Unlike continuously dust-forming WC binaries like WR 104 (ref. [8]) that are known for their 'pinwheel' nebulae, WR 140 periodically produces dust over episodes of a few months in duration and exhibits a nebular morphology resembling segmented shells[6]. This episodic dust production by WR 140 occurs when the dense stellar wind of the WC7 star is sufficiently compressed around periastron passage by the wind of the O star[6,7,10]. The dust condenses in the shock-compressed WC wind and is carried into the circumstellar medium, probably seeding the ISM with new carbonaceous dust. Given the relatively close distance of 1.64 kpc to WR 140 (refs. [12,13]), previous infrared (IR) imaging by ground-based telescopes has resolved thermal emission from (at most) two discrete, nested dust shells out to ~5,000 au from the central binary, and has provided a comparison of dust properties from one periastron passage to the next[6]. However, mid-IR spectroscopy of spatially resolved dust emission and sensitive imaging observations detecting more distant dust shells are critical to investigating the chemical composition and survival of WC dust. Such observations have been practically impossible due to the sensitivity limitations of ground-based facilities and the low angular resolution of previous space-based observatories.

As part of the James Webb Space Telescope (JWST) Director's Discretionary Early Release Science programme (ID ERS 1349), we observed WR 140 with JWST to investigate the chemical composition and survival of dust formed by colliding winds of WC binaries. WR 140 also presented an ideal target for the Director's Discretionary Early Release Science programme to demonstrate the capabilities of JWST's Mid-Infrared Instrument (MIRI) to resolve and detect faint extended emission around a bright central point source. In this Article we discuss the JWST/MIRI observations that reveal the spectral and spatial signatures of dust around WR 140: over 17 nested dust shells from the past ≥130 yr of episodic dust production and the mid-IR spectroscopic signatures from the direct emission of WC dust.

Results and discussion

WR 140 was observed by JWST with the MIRI[14–16] Medium-Resolution Spectrometer (MRS) and Imager on 2022 July 8 UT and 2022 July 27 UT, respectively. The timing of the observations captured the binary system at an orbital phase of 0.7, ~5.5 yr after its last dust-formation episode and periastron passage on 2016 December[12]. These MIRI Imager (Fig. 1, left) and MRS (Fig. 1, right) observations provide mid-infrared (5–28 μm) imaging and spectroscopy of WR 140 and its circumstellar environment that are more sensitive than previous observations by over two orders of magnitude.

The MIRI Imager observations of WR 140 at 7.7, 15 and 21 μm shown in Fig. 1 (left) reveal thermal emission from nested and remarkably evenly spaced circumstellar dust shells exceeding distances of ~45″ (~70,000 au) from the central binary. The extent of the these distant circumstellar shells detected around WR 140 exceeds that of all other known dust-forming WC systems by factors of 4 or greater[2,17,18]. The central binary and the two most recent dust shells in the Imager observations are affected by detector saturation and/or partially overlap with the point spread function (PSF) of the bright core, which is dominated by free–free emission from ionized stellar winds[6]. However, due to the dispersion of incoming light, integral field unit imaging of these inner regions with the MRS was not affected by saturation (Fig. 1, right).

One of the brightest repeating circumstellar dust features in the MIRI imaging observations is associated with the southwestern 'C1' dust emission peak, which is labelled in the MIRI MRS spectral data cube image at 8.01 μm shown in Fig. 1 (right). The C1 feature was initially identified from ground-based mid-IR imaging of WR 140 in ref. [6]. The
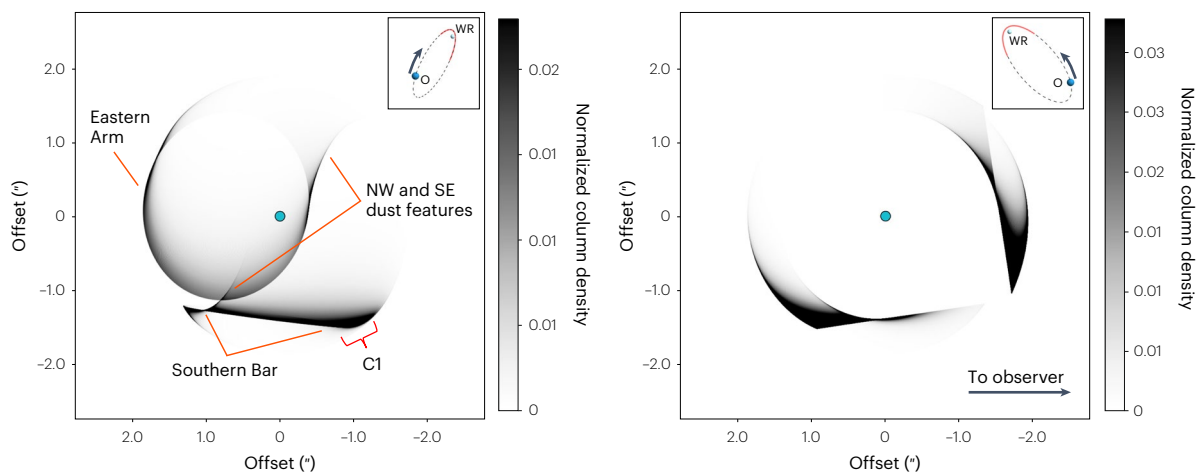
Fig. 2 | Views of the single-shell geometric dust model of WR 140 at the orbital configuration of MIRI observations. Left: dust column density in the on-sky projection of the geometric model, labelled with the observed dust features. NW, northwest; SE, southeast. Right: dust column density in the orbital-plane projection of the model. The dust column density shown has been normalized to unity by the maximum value in the each model. The cyan dot corresponds to the location of the central binary. The projected orbital configuration of WR 140 in the reference frame of the WR star and the direction of motion of the O star is shown in the insets of each projection. The semi-major axis of the orbit is 8.9 mas (14.6 au)[12]. The red regions in the orbital schematic around periastron passage correspond to true anomalies spanning −135° and +135°, where dust forms from the colliding winds (see 'WR 140 geometric models' in the Methods). Dust formation does not occur at a constant rate throughout periastron passage: more dust forms from colliding winds around the beginning and end of the orbital regions outlined in red[19].
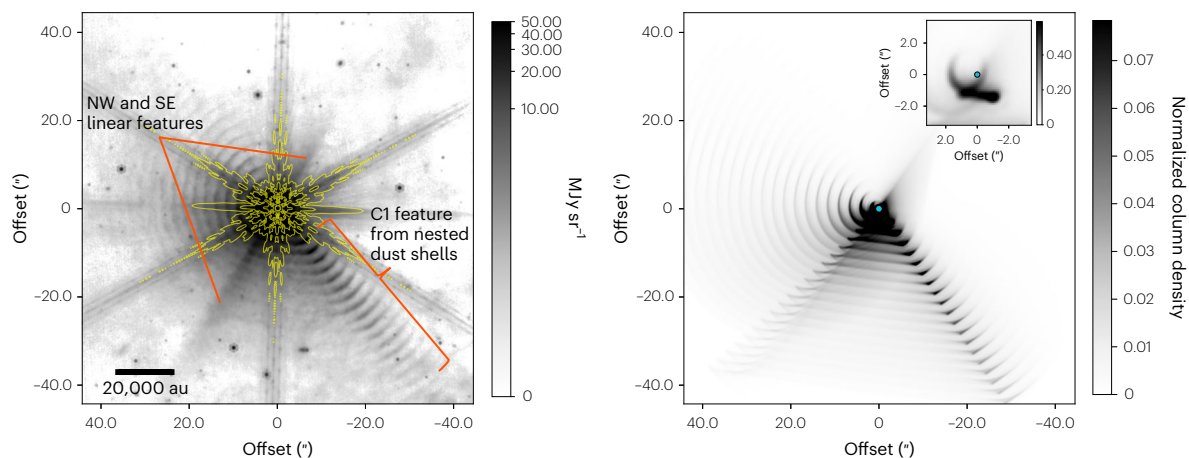

Fig. 3 | Comparison of the MIRI F1500W image of WR 140 with the 20-shell geometric dust model. Left: MIRI Imager observations of WR 140 taken with the F1500W filter. Yellow contours show the diffraction spikes from the MIRI F1500W PSF generated by WebbPSF[20] at levels corresponding to $[10^{-5}, 10^{-4}, 10^{-3}, 10^{-2}]$ times the peak intensity of the PSF. Right: dust column density model convolved with the MIRI F1500W PSF. The dust column density shown has been normalized to unity by the maximum value in the model. The inset shows roughly the inner 3″ of the dust model with the central core. The cyan dot indicates the position of the central binary.

horizontal 'Southern Bar', which extends eastwards from C1, and the curved 'Eastern Arm' are also previously identified features that show repeating structures in the MIRI imaging observations. However, the Southern Bar and Eastern Arm are not detected as far out from the central binary as C1. Eight prominent and symmetrical diffraction spikes due to the secondary struts and the hexagonal shape of JWST's primary mirror are present around the saturated core of WR 140 in the MIRI image and exhibit bluer colours than the dust emission (Fig. 1, left). Interestingly, there are two additional asymmetric and 'redder' linear features that extend from the core of WR 140 to the northwest and southeast. These linear features are not consistent with known instrumental artefacts from bright point sources, which indicates that

their origin is astrophysical and probably attributable to emission from circumstellar dust.

The observed morphology of the circumstellar dust emission around WR 140 can be interpreted by a geometric dust shell model (see 'WR 140 geometric models' in the Methods). The models were generated at an orbital phase consistent with the JWST observations to simulate the dust column density of a single dust shell (Fig. 2) as well as 20 nested dust shells (Fig. 3, right). These geometric dust shell models utilized the well-constrained measurements of WR 140's orbital parameters[10,12] and have been used previously to interpret the expansion of newly formed dust around periastron passage[19]. The single-shell model (Fig. 2) is shown in both on-sky and orbital-plane projections
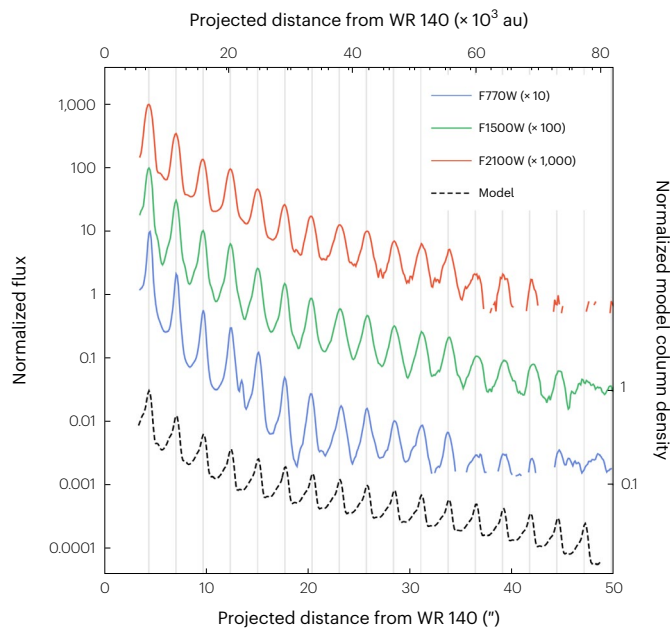
Fig. 4 | Radial plots across C1 dust features from Imager observations and the geometric dust model. Radial profiles through the C1 dust features are shown for the 7.7, 15 and 21 μm (blue, green and red lines) emission and the column density from the dust model (black, dashed line) normalized to the peak value at shell 2 and offset vertically for clarity. The lower bound of the emission is clipped at a level of 2σ. Note that the radial profiles for dust emission and column density do not match exactly because thermal dust emission is also regulated by dust temperature, which was not incorporated in the dust column density model. Grey vertical lines indicate intervals evenly spaced by 2.67″ (4,380 au), which is the median separation between the flux density peaks.

Table 1 | Projected distances of C1 features from WR 140

Shell	r_{C1}(″)	Δr_{C1}(″)	r_{C1}(au)	Δr_{C1}(au)
1	1.63	–	2,670	–
2	4.32	2.69	7,090	4,410
3	6.98	2.66	11,440	4,360
4	9.62	2.64	15,780	4,330
5	12.33	2.71	20,220	4,440
6	15.01	2.68	24,610	4,390
7	17.66	2.65	28,960	4,350
8	20.24	2.58	33,200	4,240
9	23.08	2.84	37,850	4,650
10	25.76	2.68	42,250	4,400
11	28.41	2.65	46,590	4,340
12	31.14	2.73	51,070	4,480
13	33.78	2.64	55,400	4,330
14	36.56	2.78	59,960	4,560
15	39.18	2.62	64,250	4,300
16	41.98	2.80	68,850	4,590
17	44.60	2.61	73,140	4,290

r_{C1} is the projected separation distance between C1 features and WR 140, which was calculated from the F1500W image for shells 2–17 and the MRS observation for shell 1. Δr_{C1} is the separation distance with respect to the adjacent inner dust shell adopting a distance of 1.64 kpc (refs. [12,13]).

and demonstrates how column density enhancements along the line of sight reproduce the bright dust emission features seen in the MRS observations (Fig. 1, right). Specifically, the C1 feature is composed of dust along the projected southwestern edge of the shell. Similarly, the Eastern Arm and Southern Bar arise due to enhanced column densities along the projected eastern and southern edges of the shell, respectively. Note that when WR 140 forms dust, it does not do so at a constant rate[19]. Enhanced dust formation occurs from colliding winds around the beginning and end of periastron passage, which explains the relative absence of dust to the northwest of WR 140 (Figs. 1 and 2, see 'WR 140 geometric models' in the Methods).

The 20-shell geometric model presents a striking match to the overall morphology of WR 140's nested dust shells revealed by the MIRI Imager (Fig. 3). The asymmetric and linear northwest and southeast features are present in the model at an angle and radial extent consistent with the linear features from the Imager observations. A comparison to a model MIRI F1500W PSF generated by WebbPSF[20] also demonstrates that the linear features do not align with the eight diffraction spikes (Fig. 3, left). Given the orientation of the projected northwestern and southeastern edges of the single dust shell (Fig. 2, left), the linear northwest and southeast dust features are probably associated with the projection of those edges from repeating dust shells. The model also closely reproduces the repeating bright dust features, as well as the regular spacing between the dust shells. A radial plot of the dust column density from the model and the observed dust emission in the direction of C1 from shell 2 and beyond are shown in Fig. 4 and demonstrate the consistency in the shell spacing.

The regular spacing of the observed emission from 17 shells and the agreement with the geometric model illustrate an apparently freely expanding trajectory of the dust shells and WR 140's consistent

episodic dust-production history over approximately the past 130 yr. The median separation of the first 17 dust shells along C1 is 2.67 ± 0.07″ (Table 1), which corresponds to 4,380 ± 120 au assuming a distance of 1.64 kpc to WR 140 (refs. [12,13]). The separation distance matches the expected separation given the 326 mas yr⁻¹ (2,540 km s⁻¹) proper motion of C1 (ref. [6]) over WR 140's 7.93 yr orbital period. The projected expansion velocity of the dust shells calculated from the median shell separations and the orbital period is ~2,600 km s⁻¹, which is consistent with the previously measured C1 proper motion. As the geometric models indicate that the expansion direction of the C1 feature in three-dimensional space is nearly perpendicular to our line of sight, the projected velocity of C1 should be consistent with the true dust expansion velocity[19]. The dust expansion velocity of ~2,600 km s⁻¹ is therefore slightly less than the terminal velocity of the WC-star wind (v_∞ = 2,860 km s⁻¹; ref. [21]).

The apparently constant expansion velocity of the dust shells is notable given that dust around WR 140 should experience acceleration and deceleration due to radiation pressure and drag forces, respectively[6,19]. Although beyond the scope of this work, the dust dynamics and the balance between radiation pressure and drag forces in the surrounding environment of WR 140 warrant further investigation. Given that the distant shells approach the signal-to-noise detection limits and retain a relatively constant separation distance (Fig. 4 and Table 1), fainter and cooler dust shells probably exist beyond those detected by the MIRI Imager observations. The detection of distant shells from dust production ~130 yr ago and the expected presence of more distant shells indicates that the dust formed by WR 140 can survive its harsh circumstellar environment and probably enriches the surrounding ISM. Follow-up observations with JWST of the local ISM and the surrounding ~10 pc bubble that may have been carved out by WR 140 (ref. [22]) could provide valuable insight into the ISM enrichment.

Understanding the chemical properties and spectral signatures of dust formed by WC binaries like WR 140 is important given their potential role as dust sources in the ISM (for example, refs. [1,2,17,23]).
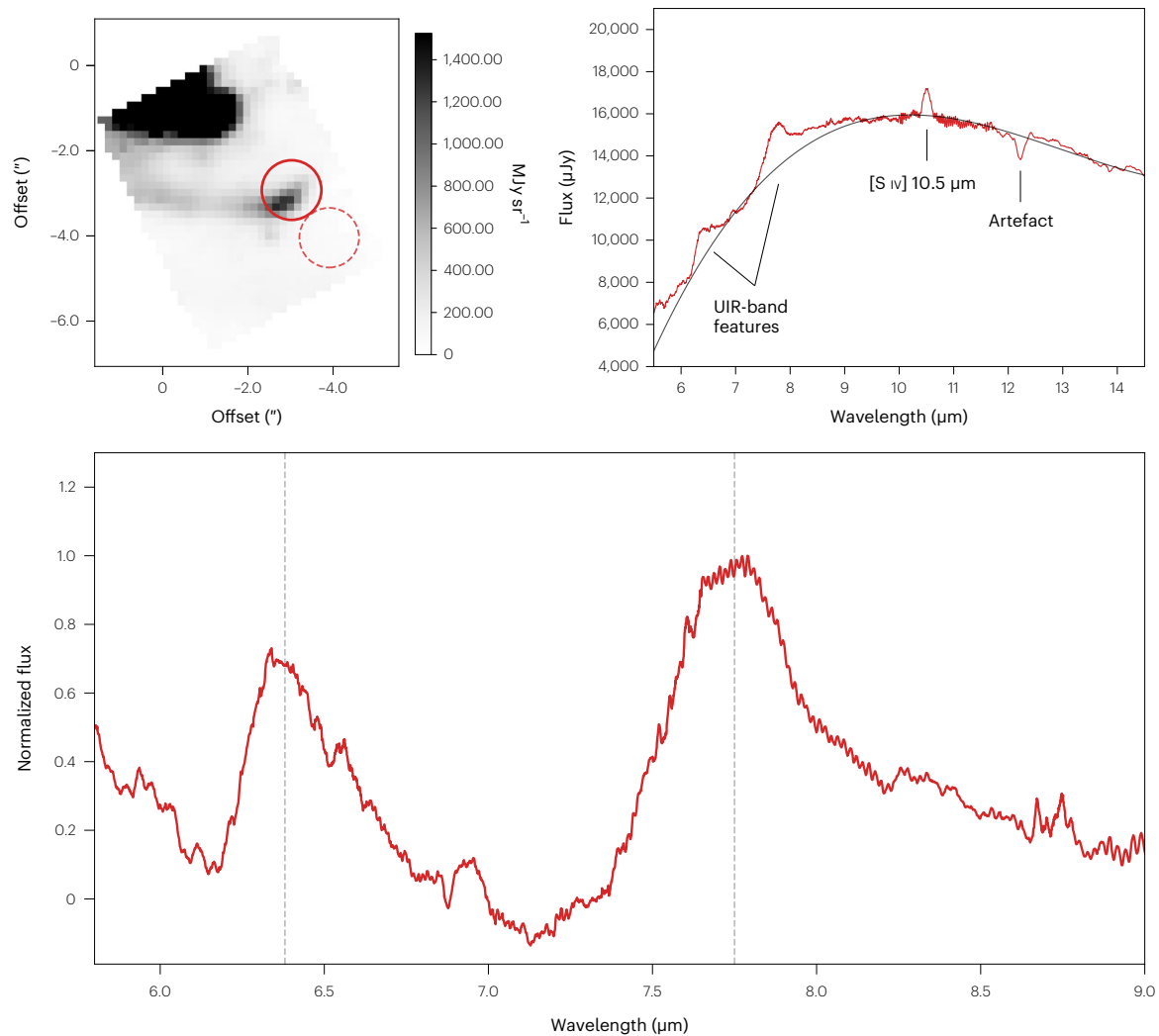
Fig. 5 | MIRI MRS spectroscopy of the C1 feature in shell 2. Top left: MRS spectral data cube image of WR 140 at 8.01 μm (Channel 2) taken at the Offset 2′ position overlaid with the apertures used to extract the spectra from the C1 feature in shell 2 (solid red circle) and measure the background emission (dashed red circle). Top right: extinction-corrected and background-subtracted 6–14 μm spectra of the C1 feature in shell 2 (red line) overlaid with the continuum fit from a cubic Chebyshev polynomial function (black line). The absorption 'feature' near 12 μm is an instrumental artefact, and the emission feature at 10.5 μm is probably emission from the [S IV] 10.5 μm fine-structure line. Bottom: 6–9 μm continuum-subtracted and normalized spectrum of the C1 feature from shell 2 exhibiting prominent 6.4 and 7.7 μm UIR-band features. Gaussian-fitted peaks of these features are located at 6.38 μm and 7.75 μm and are indicated by dashed vertical grey lines. Spectra were smoothed by convolving with a box filter kernel with a width of 21 spectral elements.

We can now investigate this using spatially and spectrally resolved observations of WR 140's circumstellar dust with the MIRI MRS. The 6–9 μm wavelength interval includes a wealth of features that trace species of interstellar molecules and dust (see ref. [24]) such as polycyclic aromatic hydrocarbons, which are believed to be carriers of the unidentified infrared (UIR) bands most commonly observed at 3.3, 6.2, 7.7, 11.2 and 12.7 μm (refs. [25–27]). Polycyclic aromatic hydrocarbons are known to be highly stable due to the honeycomb-like structure of carbon atoms fused in aromatic rings[27,28]. The survival of WR 140's circumstellar dust population in the harsh radiation field around the central binary would therefore be consistent with a composition of C-rich aromatic compounds. The presence of UIR bands that peak at 6.4 and 7.9–8.5 μm has been reported from other dust-forming WC stars[1,3,29]; however, previous spectroscopic observations were unable to spatially resolve circumstellar dust emission that blended with a bright central core. Mid-IR integral field unit spectroscopy of WR 140 with MIRI MRS can therefore be used to confirm the association of such UIR features with the WC dust.

Figure 5 presents the spectral data cube image of WR 140 at 8.01 μm, the extinction-corrected spectrum of C1 from shell 2 along with the dust-continuum fit (see 'Dust-continuum subtraction' in the Methods), and the 6–9 μm dust-continuum-subtracted and normalized spectrum from the shell 2 C1 feature. We identified the presence of two prominent UIR bands at 6.4 and 7.7 μm, which resemble the features from previous unresolved spectroscopic observations of other dust-forming WC stars. The peak positions of these features appear at 6.38 μm and 7.75 μm according to a simple Gaussian fit to the continuum-subtracted spectrum (Fig. 5, bottom). The 7.7 μm feature is typically attributed to aromatic C–C stretching modes in polycyclic aromatic hydrocarbons[27]. The 6.4 μm feature, which is primarily detected in H-poor environments from episodic dust-forming sources such as novae[30], R Coronae Borealis stars[31] and other WC stars[3], is thought to originate from large carbonaceous molecules or small, H-free carbonaceous grains[29,32]. The detection of the 6.4 μm band from circumstellar dust around WR 140 is therefore consistent with its expected H-poor environment dominated by the C-rich WC-star wind. The common

Table 2 | WR 140 MIRI observation summary

	MIRI MRS	MIRI Imager
Coordinates (J2000)	20 h 20 min 27.985 s, +43° 51′ 15.90″	2 h 20 min 27.976 s, +43° 51′ 16.28″
	20 h 20 min 27.781 s, +43° 51′ 13.05″	
Observation date (UT; MJD)	2022 July 8; MJD 59768	2022 July 27; MJD 59787
WR 140 phase (φ)	0.70	0.71
Channels/filters	Channels 1 – 4	F770W, F1500W, F2100W
Wavelength (µm)	Ch 1: 4.9–7.65	7.7, 15.0, 21.0
	Ch 2: 7.51–11.71	
	Ch 3: 11.55–18.03	
	Ch 4: 17.71–28.1	
Spectral resolving power ($\lambda/\Delta\lambda$)	1,500–3,500	0.25, 0.48, 0.67
Spaxel/pixel scale (″)	0.13–0.35	0.11
Field of view	3.2″×2.7″–6.6″×7.6″	112.6″×73.5″

The two sets of MRS coordinates correspond to the pointings of the Offset 1 and Offset 2 observations (Fig. 1, right), and the Imager coordinate indicates the pointing of the Imager observation. φ is WR 140's orbital phase at the time corresponding to the MRS and Imager observations based on the orbit described in ref. [12]. The integral field unit channels and wavelength ranges used in the MRS observations are provided, as well as the Imager filters and their corresponding central wavelengths.

8.6 µm UIR feature, which is attributed to C–H bending modes, is notably absent from the spectrum and is also consistent with an H-poor environment. The direct detection of UIR bands from shell 2 indicates that dust formed by WR 140 is carbonaceous and rich in aromatics. The stability of such aromatic compounds[27,28] supports the interpretation of WC dust survival out to the distant shells, as revealed by the Imager observations (Figs. 1 and 4).

Due to their prevalence throughout the Universe and their influence on the thermal regulation and chemistry of the ISM (see ref. [33] and ref. therein), carriers of these UIR-band features are important components of the ISM. The dominant source of UIR-band carriers has widely been thought to be evolved, solar-mass asymptotic giant branch stars[28,34]. However, the timescale for massive stars to evolve to the WR phase (millions of years) is much shorter than the timescale for lower-mass stars to evolve into asymptotic giant branch stars (≳100 Myr). On the basis of a dust-production analysis with Binary Population and Spectral Synthesis[35] models in ref. [2], the population of WC binaries could produce as much dust as the population of asymptotic giant branch stars, depending on star-formation histories and metallicities. The detection of the C1 feature out to distant shells (for example shell 17; Fig. 4) also demonstrates that the carbonaceous WC dust persists in the luminous and hard radiation field of the central binary system for at least 130 yr after the initial dust-formation event and can probably propagate to the surrounding ISM. We therefore argue that dust-forming WC binaries like WR 140 could be considered as a possible early and potentially dominant source of organic compounds and carbonaceous dust in the ISM of our Galaxy and galaxies beyond.

Methods
JWST/MIRI observations
MIRI Imager. WR 140 (J2000 RA 20 h 20 min 27.9 s, dec. +43° 51′ 16.29″; ref. [36]) was observed with the JWST/MIRI Imager on 2022 July 27 UT with the F770W, F1500W and F2100W filters in the FULL subarray mode. The Imager observations in each filter were performed using three sets of four-point dithers at starting set 5 in the positive direction with the

default pattern size that was optimized for an extended source. The FASTR1 readout pattern with 43 groups, 1 integration and 1 exposure per dither was used for each filter observation. The total exposure time in each filter was 0.40 h. A summary of the MIRI Imager observations of WR 140 is provided in Table 2.

The MIRI Imager data were processed with the JWST calibration pipeline version 1.6.2 and STCal version 1.0.0. After running the detector level pipeline, the rate file was recreated from the rateints file to ensure that the correct rate value was reported in regions that saturated after the third group. We note that a dedicated nonlinearity correction for the F2100W data was not available when we reduced this dataset. As the MIRI detectors exhibit a wavelength dependency in their nonlinear behaviour, dedicated corrections were needed at wavelengths redder than 18 µm. We therefore expected an additional error contribution of a few per cent at 21 µm.

MIRI medium-resolution spectroscopy. WR 140 was observed with the MIRI MRS[16] on 2022 July 8 UT. MIRI MRS observations provided spatially resolved spectroscopy over the four channels (Ch 1–Ch 4) that covered the 4.9–28.1 µm interval with a spectral resolving power of $R \approx 1{,}500$–3,500 (ref. [37]). Two sets of MRS observations that targeted the two most recent dust shells formed by WR 140 5.5 and 13.4 yr ago were performed (Fig. 1, right). The coordinates of the MRS observations and the other observing details are provided in Table 2. The two MRS observations were linked in a non-interruptible sequence due to the high proper motion of the circumstellar dust shells (~300 mas yr^{-1}; ref. [6]).

The first MRS observation utilized the bright core of WR 140 for target acquisition, which used the neutral density filter for 11.1 s in the FAST readout pattern. Target acquisition was not used for the second observation in the non-interruptible sequence given the small offset (~4″) required from the initial position. Each MRS observation was performed using the four-point dither optimized for an extended source and oriented in the negative direction. 60 groups and 5 integrations were used for each dither position, corresponding to 0.94 h of exposure time in each grating position (SHORT, MEDIUM, LONG). Simultaneous imaging with the MIRI Imager was also utilized in the MRS observations to improve the astrometric accuracy of the MRS data.

Calibration level 1 MIRI MRS data of WR 140 were obtained from the Mikulski Archive for Space Telescopes (MAST). These level 1 data were then processed through JWST calibration pipeline version 1.6.0, where 'output_type = band' was set in the 'cube_build' step to output 12 data cubes corresponding to the three grating positions of each of the four channels.

Data analysis
MIRI Imager background subtraction, radial dust emission profile and C1 positions. The median background emission in relatively empty patches of sky beyond the circumstellar shells in the F770W, F1500W and F2100W MIRI Imager observation exhibited fluxes of 10.4, 41.4 and 210.2 MJy sr^{-1}, respectively. A background subtraction using the median values was therefore applied to the three MIRI Imager observations.

A radial 3-pixel-width line-cut plot originating at the position of WR 140 and oriented 53° south of west was used to measure the emission and positions of the C1 features from the MIRI Imager observations (Fig. 4; Table 1). A Gaussian profile was used to measure the peak positions of each of shells 2–17 from the radial dust emission profile of the F1500W image. An identical line cut was used to measure the dust column density from the 20-shell geometric dust model.

MIRI MRS spectroscopy of C1. Spectra were extracted from the MIRI MRS 'Offset 1' observations of C1 in shell 1 (20 h 20 min 27.838 s, +43° 51′ 14.69″) using a circular aperture with a radius $r = 0.7″$. Subtraction of the background emission and contamination from the diffraction pattern of the bright core was performed by using a circular aperture in a relatively dust-free position northwest of WR 140 (20 h

20 min 27.932 s, +43° 51′ 17.75″) at the same separation distance from the C1 aperture. However, contamination from emission lines from the bright stellar core seemed to persist in the shell 1 C1 spectra even after background subtraction. Follow-up work from the WR Dust-ERS programme (ERS 1349) will be conducted to implement a technique to perform PSF subtraction on the MIRI MRS observations in a future study.

A circular aperture of $r = 0.7″$ was also used to extract the spectra from the MIRI MRS 'Offset 2' observations of C1 in shell 2 (20 h 20 min 27.657 s, +43° 51′ 12.970″). Background emission for the C1 region in shell 2 was measured and subtracted using a circular background aperture with an identical radius centred on a relatively empty area in the field of view to the southwest of shell 2 at the following coordinates: 20 h 20 min 27.575 s, +43° 51′ 11.852″. The 6.4 and 7.7 μm features were present in background-subtracted spectra even when using different background positions in other relatively empty regions of the sky.

To mitigate high-frequency noise from artefacts such as 'fringing', the MRS spectra were smoothed by convolving with a box filter kernel that had a width of 21 spectral elements ($\Delta\lambda = 0.04$ μm). The width of the UIR features ($\gtrsim 0.2$ μm) was notably larger than the width of the kernel used for smoothing.

Spectral stitching between MRS channels. To combine the spectra extracted from the three subbands from channels 1–4, the median flux density in the overlapping wavelengths between the 12 subbands was used to combine the extracted C1 spectra. The spectra were normalized to the Channel 2 SHORT subband ($\lambda = 7.51$–8.76 μm), which overlaps with the 6–9 μm wavelength range studied in this work.

Dust-continuum subtraction. The dust-continuum emission was fitted and subtracted from the ~6–9 μm wavelength range of the extracted spectra of the C1 region from shell 2 using a cubic Chebyshev polynomial function from the 'Spectrum1D' and 'fit_continuum' functions in the Python package specutils[38]. Wavelengths between 6.8–7.2 μm and 9–15 μm were used to fit the C1 continuum in shell 2. Ionized gas probably attributable to the [S IV] 10.5 μm fine-structure line was also detected in the C1 spectra and will be investigated in future analysis. The apparent absorption 'feature' near 12 μm was an instrumental artefact. The shorter wavelengths ($\lambda \lesssim 6$ μm) were omitted for the shell 2 dust-continuum fit to avoid enhanced emission probably arising from a hotter dust component (R.M.L. et al., manuscript in preparation). The C1 spectra from shell 2 and the dust-continuum fit are shown in Fig. 5 (top right). The ~6–14 μm continuum-subtracted spectra were then normalized to the peak flux density of the 7.7 μm feature (Fig. 5, bottom).

Extinction correction. Extracted MIRI MRS spectra from the circumstellar dust around WR 140 were dereddened using the extinction correction factors derived from the Galactic interstellar extinction curve from Gordon et al.[39], where the optical total-to-selective extinction ratio (R_V) is 3.17 and the extinction at the K_s-band is $A_{K_s} = 0.24$ (ref. [13]).

WR 140 geometric models
The circumstellar dust structures around WR 140 shown in Fig. 3 (left) were simulated using the geometric model presented in ref. [19]. The model assumes dust to be produced on a thin, conical surface originating from the wind-shock interface and has been applied in previous studies of dust-forming colliding-wind binaries[17,40,18]. The geometry of the dust structure depends in part on the orbit of the binary, for which we adopted the well-constrained orbital parameters from ref. [12]. The half opening angle of the conical dust surface was assumed to be 40° (refs. [6,19,41]), and the dust expansion velocity was assumed to be 2,600 km s^{-1}, which was consistent with the velocity measured from the separation distance between the dust shells (Table 1). The only parameter of the geometric model that deviated from the original model fitted

to ground-based observations of a single shell from ref. [19] was the dust expansion speed, which was slightly larger than the expansion speed of 2,450 km s^{-1} fitted to data at an earlier orbital phase (0.592). This apparent discrepancy may reflect acceleration during the expansion of the dust plume found by ref. [19]. The model was then convolved with the F1500W MIRI Imager PSF from the WebbPSF Python package[20]. Note that because only the dust morphology was generated by the model, the central binary itself did not appear.

Observations of WR 140 indicate that dust does not form evenly over the orbit[6,19]. By fitting to the structures in one shell of dust observed by ground-based AO-assisted IR imaging, ref. [19] found that the structures were reproduced if dust production from the colliding winds began at a true anomaly of −135° and ceased at +135° (Fig. 2), between which dust production was suppressed. No dust was assumed to be produced along other parts of the orbit. Furthermore, the structures were better reproduced when it was assumed that the dust density peaked on the trailing edge of the conical shock front, becoming progressively lower when moving towards the leading edge. Further details of the geometric model of WR 140 are provided in ref. [19].

Data availability
Data used in this study were obtained under JWST Director's Discretionary Early Release Science programme ID ERS 1349 and have no exclusive access period. Data can be obtained from the Mikulski Archive for Space Telescopes (MAST; https://archive.stsci.edu/missions-and-data/jwst).

Code availability
This research made use of Astropy, a community-developed core Python package for Astronomy[42]. This research also made use of Jdaviz, which is a package of astronomical data analysis visualization tools based on the Jupyter platform[43].

References
1. Marchenko, S. V. & Moffat, A. F. J. Search for polycyclic aromatic hydrocarbons in the outflows from dust-producing Wolf-Rayet stars. *Mon. Not. R. Astron. Soc.* **468**, 2416–2428 (2017).
2. Lau, R. M. et al. Revisiting the impact of dust production from carbon-rich Wolf-Rayet binaries. *Astrophys. J.* **898**, 74 (2020).
3. Endo, I. et al. Detection of a Broad 8 μm UIR feature in the mid-infrared spectrum of WR 125 observed with Subaru/COMICS. *Astrophys. J.* **930**, 116 (2022).
4. Crowther, P. A. Physical properties of Wolf-Rayet stars. *Annu. Rev. Astron. Astrophys.* **45**, 177–219 (2007).
5. Usov, V. V. Stellar wind collision and dust formation in long-period, heavily interacting Wolf-Rayet binaries. *Mon. Not. R. Astron. Soc.* **252**, 49–52 (1991).
6. Williams, P. M. et al. Orbitally modulated dust formation by the WC7+O5 colliding-wind binary WR140. *Mon. Not. R. Astron. Soc.* **395**, 1749–1767 (2009).
7. Eatson, J. W., Pittard, J. M. & Van Loo, S. Exploring dust growth in the episodic WCd system WR140. Preprint at https://arxiv.org/abs/2204.12354 (2022).
8. Tuthill, P. G., Monnier, J. D. & Danchi, W. C. A dusty pinwheel nebula around the massive star WR104. *Nature* **398**, 487–489 (1999).
9. Cherchneff, I., Le Teuff, Y. H., Williams, P. M. & Tielens, A. G. G. M. Dust formation in carbon-rich Wolf-Rayet stars. I. Chemistry of small carbon clusters and silicon species. *Astron. Astrophys.* **357**, 572–580 (2000).
10. Monnier, J. D. et al. First visual orbit for the prototypical colliding-wind Binary WR 140. *Astrophys. J. Lett.* **742**, L1 (2011).
11. Fahed, R. et al. Spectroscopy of the archetype colliding-wind binary WR 140 during the 2009 January periastron passage. *Mon. Not. R. Astron. Soc.* **418**, 2–13 (2011).

12. Thomas, J. D. et al. The orbit and stellar masses of the archetype colliding-wind binary WR 140. *Mon. Not. R. Astron. Soc.* **504**, 5221–5230 (2021).

13. Rate, G. & Crowther, P. A. Unlocking galactic Wolf-Rayet stars with Gaia DR2 - I. Distances and absolute magnitudes. *Mon. Not. R. Astron. Soc.* **493**, 1512–1529 (2020).

14. Bouchet, P. et al. The Mid-Infrared Instrument for the James Webb Space Telescope, III: MIRIM, the MIRI Imager. *Publ. Astron. Soc. Pac.* **127**, 612 (2015).

15. Wright, G. S. et al. The Mid-Infrared Instrument for the James Webb Space Telescope, II: design and build. *Publ. Astron. Soc. Pac.* **127**, 595 (2015).

16. Wells, M. et al. The Mid-Infrared Instrument for the James Webb Space Telescope, VI: the Medium Resolution Spectrometer. *Publ. Astron. Soc. Pac.* **127**, 646 (2015).

17. Lau, R. M. et al. Resolving decades of periodic spirals from the Wolf-Rayet dust factory WR 112. *Astrophys. J.* **900**, 190 (2020).

18. Han, Y. et al. The extreme colliding-wind system Apep: resolved imagery of the central binary and dust plume in the infrared. *Mon. Not. R. Astron. Soc.* **498**, 5604–5619 (2020).

19. Han, Y., Tuthill, P. G., Lau, R. M. & Soulain, A. Radiation driven acceleration in the expanding WR140 dust shell. *Nature* (2022); https://doi.org/10.1038/s41586-022-05155-5

20. Perrin, M. D. et al. Updated point spread function simulations for JWST with WebbPSF. In *Space Telescopes and Instrumentation 2014: Optical, Infrared, and Millimeter Wave* SPIE Conference Series Vol. 9143 (eds Oschmann, J. et al.) 91433X (SPIE, 2014).

21. Williams, P. M. & Eenens, P. R. J. Displaced He I absorption lines in Wolf-Rayet stars : revisions to v-infinite. *Mon. Not. R. Astron. Soc.* **240**, 445–457 (1989).

22. Arnal, E. M. A high-resolution H I study of the interstellar medium local to HD 193793. *Astron. J.* **121**, 413–425 (2001).

23. Lau, R. M. et al. Revealing efficient dust formation at low metallicity in extragalactic carbon-rich Wolf-Rayet binaries. *Astrophys. J.* **909**, 113 (2021).

24. Peeters, E. et al. The rich 6 to 9 μm spectrum of interstellar PAHs. *Astron. Astrophys.* **390**, 1089–1113 (2002).

25. Leger, A. & Puget, J. L. Identification of the unidentified infrared emission features of interstellar dust. *Astron. Astrophys.* **137**, L5–L8 (1984).

26. Allamandola, L. J., Tielens, A. G. G. M. & Barker, J. R. Polycyclic aromatic hydrocarbons and the unidentified infrared emission bands: auto exhaust along the milky way. *Astrophys. J. Lett.* **290**, L25–L28 (1985).

27. Tielens, A. G. G. M. Interstellar polycyclic aromatic hydrocarbon molecules. *Annu. Rev. Astron. Astrophys.* **46**, 289–337 (2008).

28. Allamandola, L. J., Tielens, A. G. G. M. & Barker, J. R. Interstellar polycyclic aromatic hydrocarbons: the infrared emission bands, the excitation/emission mechanism, and the astrophysical implications. *Astrophys. J. Suppl. Ser.* **71**, 733 (1989).

29. Chiar, J. E., Peeters, E. & Tielens, A. G. G. M. The infrared emission features in the spectrum of the Wolf-Rayet star WR 48a. *Astrophys. J. Lett.* **579**, L91–L94 (2002).

30. Helton, L. A., Evans, A., Woodward, C. E. & Gehrz, R. D. Atypical dust species in the ejecta of classical novae. In *EAS Publications Series Vol. 46, PAHs and the Universe: A Symposium to Celebrate the 25th Anniversary of the PAH Hypothesis* (eds Joblin, C. & Tielens, A. G. G. M.) 407–412 (EAS, 2011).

31. García-Hernández, D. A., Rao, N. K. & Lambert, D. L. Dust around R Coronae Borealis stars. II. Infrared emission features in an H-poor environment. *Astrophys. J.* **773**, 107 (2013).

32. Harrington, J. P., Lame, N. J., Borkowski, K. J., Bregman, J. D. & Tsvetanov, Z. I. Discovery of a 6.4 micron dust feature in hydrogen-poor planetary nebulae. *Astrophys. J. Lett.* **501**, L123–L126 (1998).

33. Li, A. Spitzer's perspective of polycyclic aromatic hydrocarbons in galaxies. *Nat. Astron.* **4**, 339–351 (2020).

34. Galliano, F., Dwek, E. & Chanial, P. Stellar evolutionary effects on the abundances of polycyclic aromatic hydrocarbons and supernova-condensed dust in galaxies. *Astrophys. J.* **672**, 214–243 (2008).

35. Eldridge, J. J. et al. Binary Population and Spectral Synthesis version 2.1: construction, observational verification, and new results. *Publ. Astron. Soc. Aust.* **34**, e058 (2017).

36. Lindegren, L. et al. Gaia Early Data Release 3. The astrometric solution. *Astron. Astrophys.* **649**, A2 (2021).

37. Labiano, A. et al. Wavelength calibration and resolving power of the JWST MIRI Medium Resolution Spectrometer. *Astron. Astrophys.* **656**, A57 (2021).

38. Earl, N. et al. astropy/specutils: V1.7.0. *Zenodo* (2022); https://doi.org/10.5281/zenodo.6207491

39. Gordon, K. D. et al. Milky Way mid-infrared Spitzer spectroscopic extinction curves: continuum and silicate features. *Astrophys. J.* **916**, 33 (2021).

40. Callingham, J. R. et al. Anisotropic winds in a Wolf-Rayet binary identify a potential gamma-ray burst progenitor. *Nat. Astron.* **3**, 82–87 (2019).

41. Marchenko, S. V. et al. The unusual 2001 periastron passage in the "clockwork" colliding-wind binary WR 140. *Astrophys. J.* **596**, 1295–1304 (2003).

42. Astropy Collaboration. The Astropy Project: building an open-science project and status of the v2.0 core package. *Astron. J.* **156**, 123 (2018).

43. Lim, P. L. et al. spacetelescope/jdaviz: v2.8.0. *Zenodo* (2022); https://doi.org/10.5281/zenodo.6877878

Author contributions

R.M.L. led the analysis and is PI of the WR DustERS Team. R.M.L. and M.J.H. conceived and designed the project. I.A. and D.R.L. processed the MRS data, and M.G.M. processed the MIRI imaging data. Y.H.

and P.T. constructed the geometric models of WR 140. All authors contributed to observation planning and/or scientific interpretation as members of the WR DustERS Team.

Competing interests

The authors declare no competing interests.

Additional information

Correspondence and requests for materials should be addressed to Ryan M. Lau.

Peer review information *Nature Astronomy* thanks Paul Crowther, Joseph Callingham and the other, anonymous, reviewer(s) for their contribution to the peer review of this work.

Reprints and permissions information is available at www.nature.com/reprints.

Publisher's note Springer Nature remains neutral with regard to jurisdictional claims in published maps and institutional affiliations.

¹NOIRLab, NSF, Tucson, AZ, USA. ²Arkansas Tech University, Russellville, AR, USA. ³Institute of Astronomy, University of Cambridge, Cambridge, UK. ⁴Instituut voor Sterrenkunde, KU Leuven, Leuven, Belgium. ⁵CRESST II and X-ray Astrophysics Laboratory, NASA/GSFC, Greenbelt, MD, USA. ⁶Institute for Astrophysics and Computational Sciences, The Catholic University of America, Washington, DC, USA. ⁷Department of Physics, University of Auckland, Auckland, New Zealand. ⁸Department of Astronomy, School of Science, University of Tokyo, Tokyo, Japan. ⁹Space Telescope Science Institute, Baltimore, MD, USA. ¹⁰European Space Agency, Madrid, Spain. ¹¹Space Telescope and Science Institute, Baltimore, MD, USA. ¹²Exoplanets and Stellar Astrophysics Laboratory, NASA/GSFC, Greenbelt, MD, USA. ¹³UK Astronomy Technology Centre, Royal Observatory, Edinburgh, UK. ¹⁴Department of Physics, University of Maryland, Baltimore County, Baltimore, MD, USA. ¹⁵Université Côte d'Azur, Observatoire de la Côte d'Azur, CNRS, Laboratoire Lagrange, Nice, France. ¹⁶Université Côte d'Azur, Observatoire de la Côte d'Azur, CNRS, Laboratoire Artémis, Nice, France. ¹⁷Department of Physics and Astronomy, San Jose State University, San Jose, CA, USA. ¹⁸Science Systems and Applications Inc., Lanham, MD, USA. ¹⁹NASA/GSFC, Greenbelt, MD, USA. ²⁰Institute of Space and Astronautical Science, Japan Aerospace Exploration Agency, Sagamihara, Japan. ²¹Département de physique, Université de Montréal, Montreal, Quebec, Canada. ²²Centre de Recherche en Astrophysique du Québec, Montreal, Quebec, Canada. ²³Department of Physics and Astronomy, University of California, Los Angeles, CA, USA. ²⁴Caltech/IPAC, Pasadena, CA, USA. ²⁵Department of Physics, Faculty of Science and Engineering, Meisei University, Tokyo, Japan. ²⁶Jet Propulsion Laboratory, California Institute of Technology, Pasadena, CA, USA. ²⁷Department of Physics and Astronomy, Embry-Riddle Aeronautical University, Prescott, AZ, USA. ²⁸Department of Physics and Astronomy, Bartol Research Institute, University of Delaware, Newark, DE, USA. ²⁹Instituto de Astronomía, Universidad Nacional Autónoma de México, Mexico City, Mexico. ³⁰Max-Planck-Institut für Astronomie, Heidelberg, Germany. ³¹Department of Astronomy, University of Arizona, Tucson, AZ, USA. ³²Université Grenoble Alpes, CNRS, IPAG, Grenoble, France. ³³School of Physics and Astronomy, University of Birmingham, Birmingham, UK. ³⁴Sydney Institute for Astronomy, School of Physics, University of Sydney, Sydney, New South Wales, Australia. ³⁵Max Planck Institute for Radio Astronomy, Bonn, Germany. ³⁶Institute for Astronomy, University of Edinburgh, Royal Observatory, Edinburgh, UK. 37Graduate School of Science and Technology, Tokyo Institute of Technology, Tokyo, Japan. ✉e-mail: ryan.lau@noirlab.edu